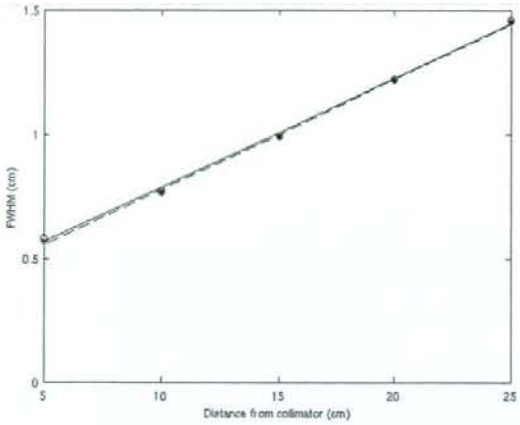

Fig. 2 Full width at half maximum as a function of distance from the collimator for ^{99m}Tc and ^{123}I. ^{99m}Tc measurements are shown with *circles* and the linear model fit (Eq. 2) as *solid line*, whereas ^{123}I measurements are presented with *stars* and the linear model fit as *dashed line*. The parameters α and β in Eq. 2 for ^{99m}Tc were 0.35 and 0.04 and for ^{123}I 0.33 and 0.04, respectively

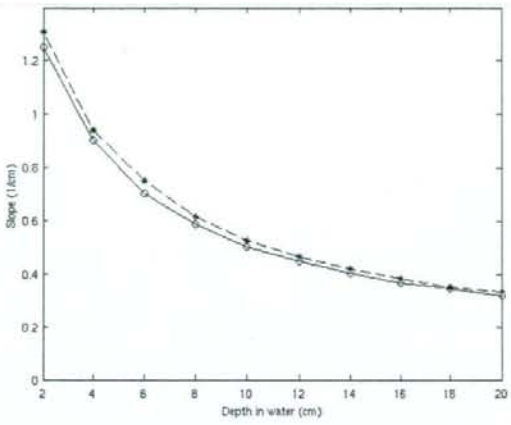

Fig. 3 Scatter kernel slope as a function of depth in water for ^{99m}Tc and ^{123}I. ^{99m}Tc measurements are shown with *solid line* with *circles* and ^{123}I measurements using *dashed line* with *stars*

high-resolution parallel hole collimator with 0.14 cm in hole diameter, a hole length of 2.7 cm, and a septal thickness of 0.018 cm was used. The pixel size in the simulations was set to 0.2 cm, and the projection data were acquired into a 128 × 128 matrix. Two sets of simulations were performed using ^{99m}Tc and ^{123}I as radionuclides. Symmetrical 15% energy window was centered on the photo-peak. For ^{123}I high-energy photons were not included in the simulations.

The FWHM as a function of distance was obtained by simulating point sources in air at different distances (5 cm, 10 cm, 15 cm, 20 cm, and 25 cm) from the collimator. FWHM was calculated by fitting a Gaussian function to a profile drawn through the center of the image, and the intercept (α) and slope (β) in Eq. 2 were obtained by fitting the linear model to the measurements (see Fig. 2).

The scatter kernel slope [$\alpha(d_{tis})$] for the reconstruction-based scatter-correction methods (Hutton's method and new method) was obtained by simulating a line source behind slabs of different thickness (2 cm, 4 cm, 6 cm, 8 cm, 10 cm, 12 cm, 14 cm, 16 cm, 18 cm, and 20 cm) of water. Low noise level planar images of the line sources were acquired and the slopes were calculated by fitting exponential functions to the scatter tails of profiles drawn through the center of the image. The results of this experiment are presented in Fig. 3. The slope for each plane at different depths in tissue in the reconstruction-based scatter correction was obtained by linear interpolation from the measurements. The slope for depth-independent scatter kernel in the conventional TDCS was set to 0.45 l/cm for ^{99m}Tc and 0.47 l/cm for ^{123}I.

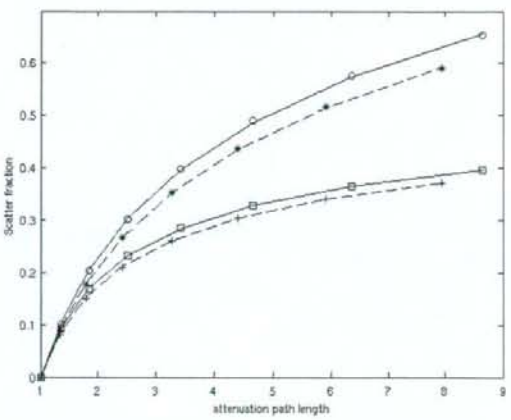

Fig. 4 Scatter fractions as a function of attenuation path length for ^{99m}Tc and ^{124}I. Scatter-to-primary ^{99m}Tc measurements are shown with *circles*, scatter-to-primary ^{124}I measurements with *stars*, scatter-to-total ^{99m}Tc measurements with *squares*, and scatter-to-total ^{124}I measurements are presented with plusses. The build-up equation fit (Eqs. 3, 4) for ^{99m}Tc is shown with *solid line* and for ^{123}I as *dashed line*. The build-up equation parameters *A*, *B*, and γ were 3.6, 2.6, and 0.13 for ^{99m}Tc and 4.3, 3.3, and 0.09 for ^{123}I. The same *A*, *B*, and γ parameters fitted well in both Eqs. 3 and 4

The *A*, *B*, and γ scatter-fraction coefficients were calculated by simulating point sources behind slabs of different thicknesses (2 cm, 4 cm, 6 cm, 8 cm, 10 cm, 12 cm, and 14 cm) of water. The scatter fractions were obtained from SIMIND, and these measurements were

fitted to Eqs. 3 and 4. Results from this experiment are presented in Fig. 4.

Brain phantom simulations

The new reconstruction-based scatter-correction method was compared with that of Hutton's method and to TDCS using the Zubal brain phantom [15]. The phantom was modified to represent the uptake of ^{99m}Tc-ECD (gray-to-white matter ratio 2.5:1) and ^{123}I-FP-CIT (striatum-to-background ratio 4:1). SIMIND was used to create low noise projection data of the phantoms, 120 angles over 360° circular orbit, by simulating approximately 70 MCts/projection using the same parameters as was used in determining the parameters for the reconstruction algorithms with the exception that pixel size was now 0.225 cm. Attenuation map was created by assigning correct densities for brain tissue and skull. The low-noise projections were then used to create noisy projection sets containing a total of 5 MCts for the ^{99m}Tc-ECD and 2 MCts for the ^{123}I-FP-CIT, which represent the average total count levels of ^{99m}Tc-ECD and ^{123}I-FP-CIT in clinical studies (personal communication Prof. Jyrki T. Kuikka, Kuopio University Hospital, Finland).

The noisy projection data were reconstructed using the new algorithm with (4 iterations and 15 subsets) and without collimator modeling (2 iterations and 15 subsets) and the GM projections with/without TDCS (2 iterations and 10 subsets). Reconstructions with collimator modeling used more iterations because of their slower convergence. Both reconstructions according to Hutton's method were performed with 2 iterations and 15 subsets. All the reconstructed images were post-filtered using a 3D Butterworth filter (cut-off 1.0 cycles/cm, order 5) according to clinical practice. The accuracy of the reconstruction methods was studied by comparing the overall accuracy of the reconstruction and correction methods and by calculating the normalized mean-squared error (NMSE) with respect to the known true counts (f_j^{true}):

$$\text{NMSE} = \frac{\sum_j \left(f_j^{\text{true}} - f_j\right)^2}{\sum_j f_j^{\text{true}^2}} \tag{6}$$

and the average gray-to-white matter and striatum-to-background ratios.

Results

Results of the Zubal brain phantom experiments are shown in Table 1. As can be seen, the reconstruction-based scatter-correction methods outperform the conventional TDCS in terms of contrast (gray-to-white matter and striatum-to-background ratios) and quantitative accuracy (normalized mean-squared errors). The new method is more accurate than that of Hutton's one, but the difference between the two is small. Highest accuracy is achieved when collimator-blurring correction is also applied during reconstruction. Indeed, collimator-blurring compensation might prove to be very useful in quantitative brain studies because it clearly reduces the partial volume effect offering higher accuracy. Interestingly, reconstructions from GM projections with only attenuation correction perform worse than reconstructions from normal projections. This is primarily caused by differences in attenuation correction. GM projections require projection space attenuation correction, whereas more accurate reconstruction space attenuation correction can be performed with normal projections. Examples of images with different reconstruction methods are shown in Figs. 5 and 6. The reconstruction-based scatter-compensation methods provide slightly better image quality than TDCS and the best result is obtained when collimator-blurring correction is also applied.

Table 1 Normalized mean-squared error (NMSE), gray-to-white matter ratio (GM:WM), and striatum-to-background ratio (STR:BG) for the ^{99m}Tc-ECD and ^{123}I-FP-CIT simulation studies

Corrections	NMSE_{ECD}	GM:WM	$\text{NMSE}_{\text{FP-CIT}}$	STR:BG
Attenuation*	0.186/0.182	1.11/1.17	0.136/0.134	2.19/2.24
Attenuation + $\text{scatter}_{\text{TDCS}}$	0.179	1.15	0.134	2.27
Attenuation + $\text{scatter}_{\text{Hutton}}$	0.173	1.24	0.127	2.29
Attenuation + $\text{scatter}_{\text{New}}$	0.172	1.25	0.126	2.29
Attenuation + $\text{scatter}_{\text{New}}$ + CDR	0.165	1.41	0.121	2.48

Results are presented for ordered subsets expectation maximization (OSEM) reconstruction with only attenuation correction, with attenuation and scatter correction [transmission-dependent convolution subtraction (TDCS)-based, Hutton's method and new method] and with attenuation, new scatter, and collimator-blurring correction (CDR). The attenuation correction only results are presented for two algorithms: geometric mean (GM) projection OSEM reconstruction, which has to be used for TDCS-based scatter correction and normal OSEM reconstruction which is used for Hutton's and new scatter-compensation methods

*The first values shown are the results of GM projection reconstruction and the second the results of normal reconstruction

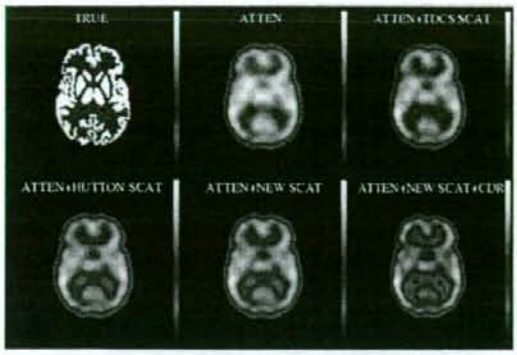

Fig. 5 Representative slices of the ^{99m}Tc-ECD study obtained with ordered subsets expectation maximization (OSEM) using only attenuation correction (reconstruction with normal projections), attenuation + transmission-dependent convolution subtraction (TDCS)-based scatter correction, attenuation + Hutton's scatter correction, attenuation + new scatter correction, and attenuation + new scatter + collimator-blurring (CDR) correction

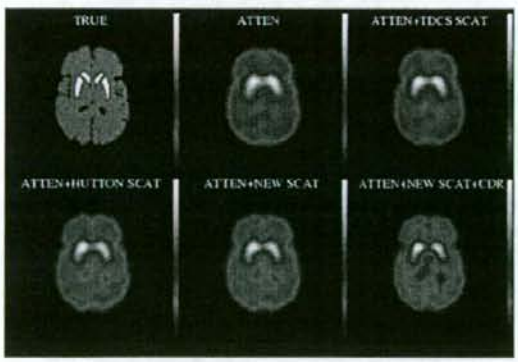

Fig. 6 Representative slices of the ^{123}I-FP-CIT study obtained with OSEM using only attenuation correction (reconstruction with normal projections), attenuation + TDCS-based scatter correction, attenuation + Hutton's scatter correction, attenuation + new scatter correction, and attenuation + new scatter + CDR correction

The average reconstruction times of the ^{99m}Tc-ECD and ^{123}I-FP-CIT Zubal phantom experiments are listed in Table 2. The TDCS is much faster than other methods, but it is worth noting that because of the GM projections TDCS uses only 60 projections in reconstruction, whereas the new method uses 120 projection images. TDCS also applies projection-based attenuation modeling as explained earlier, and therefore it does not require rotation of the attenuation map during the reconstruction, which saves time. Hutton's method is by far the slowest one because it requires pre-reconstruction to calculate scatter projections, but when the scatter projections are ready the actual scatter correction in the final reconstruction is faster than scatter compensation with the new method.

Table 2 Average reconstruction times for the ^{99m}Tc-ECD and ^{123}I-FP-CIT studies

Corrections	Time per iteration (s)
Attenuation[a]	67/212
Attenuation + scatter$_{TDCS}$	67
Attenuation + scatter$_{Hutton}$	560 + 212
Attenuation + scatter$_{New}$	254
Attenuation + scatter$_{New}$ + CDR	336

Results are presented for OSEM reconstruction with only attenuation correction, with attenuation and scatter correction (TDCS-based, Hutton's method and new method) and with attenuation, new scatter, and collimator-blurring correction (CDR). The attenuation correction only results are presented for two algorithms: geometric mean (GM) projection OSEM reconstruction, which has to be used for TDCS-based scatter correction and normal OSEM reconstruction which is used for Hutton's and new scatter-compensation method. Calculation times have been obtained using 1.7 GHz Pentium processor with 1 GB RAM

[a] The first value shown is the time for GM projection reconstruction and the second is for normal reconstruction

[b] Pre-reconstruction and scatter forwardprojection calculation time + time for single iteration for the final reconstruction

Discussion

Here, we implemented a 3D reconstruction algorithm with transmission-dependent scatter modeling for efficient reconstruction-based scatter correction and compared it with reconstruction-based scatter-compensation method presented by Hutton et al. [7, 8], and with the conventional TDCS-based scatter-correction method [4]. The new algorithm proved to provide the highest accuracy according to Monte Carlo simulation studies of Zubal brain phantom (see Table 1). The new algorithm is also very advantageous because it allows easy incorporation of accurate attenuation and collimator-blurring corrections, which might prove to be very useful in high-quality SPECT imaging.

The presented scatter-correction method is relatively easy to implement and use. It requires two measurements for calibration: line source measurement to determine the scatter kernel slopes and point source measurement to determine the scatter fractions. These measurements need to be performed once for each radionuclide and collimator pair. In fact for lower-energy isotopes such as ^{99m}Tc, the scatter fractions have shown to be collimator independent [16] and therefore a single measurement might be sufficient for scatter-correction calibration for a large family of different collimators.

In addition to the ease of implementation, the execution time is of importance if a reconstruction method is to be used in clinical practice. Table 2 lists the calculation times per iteration for the scatter-correction methods. The TDCS-based scatter correction is clearly the fastest method, but the new method does not provide an extensive increase in computation time when compared with reconstruction without scatter correction. It is worth pointing out that even though the new method was accelerated using the coarse-grid scatter modeling, the reconstruction algorithm itself is not yet fully optimized. We believe that by further optimizing the structure of our reconstruction code and by replacing the current bilinear interpolation-based reconstruction grid rotation with a faster three-pass shear [17] method, we can still greatly reduce the computation time from the current 336 s/iteration.

This study has some limitations. First, testing and comparison of algorithms was performed using simplified simulated data. Simulated data were chosen, because they allowed easy comparison with true activity distributions, which are beneficial to finding small errors in initial reconstruction experiments. Simulations were performed as Monte Carlo simulations, which are known to have relatively good correspondence with real clinical data and we also tried to closely mimic clinical-imaging situations using appropriate noise levels and post-filters. On the other hand, it should be realized that even Monte Carlo simulations will probably produce results that are too good owing to the absence of errors in energy window calibration, non-uniformities, and so on that often hamper the quality of clinical data. Moreover, the high-energy photons of ^{123}I, which can penetrate or scatter at the collimator, were not included in the simulations, and the reconstructions were performed with noise-free and perfectly aligned attenuation maps. Both of these conditions are unnatural and their effects have to be investigated in detail in further studies.

Second, the metrics (NMSE and activity ratios) that were used to analyze the reconstructed images are simplistic, and more clinically relevant measures such as cerebral blood flow, binding potential, or task-based measures such as lesion detection are required in future studies to evaluate the true benefits of the presented reconstruction and corrections methods. Comparison of the new transmission-dependent scatter correction with other reconstruction-based scatter-correction methods such as in Beekman et al. [18] and Frey et al. [19] would also make an interesting topic for a further investigation.

In summary, we have proposed a 3D reconstruction algorithm with attenuation, collimator blurring, and transmission-dependent scatter correction, which shows promise as an efficient and accurate reconstruction method; however, further testing is still required to evaluate its true applicability in the clinical setting.

Acknowledgment This work was supported by grants from the Japan Society for the Promotion of Science.

References

1. Buvat I, Rodriguez-Villafuerte M, Todd-Pokropek A, Benali H, Di Paola R. Comparative assessment of nine scatter correction methods based on spectral analysis using Monte Carlo simulations. J Nucl Med 1995;36:1476–88.
2. Frey EC, Tsui BMW, Ljungberg M. A comparison of scatter compensation methods in SPECT: subtraction-based techniques versus iterative reconstruction with accurate modeling of the scatter response. Conference Record of the 1992 Nuclear Science Symposium and Medical Imaging Conference 1992;2: 1035–7.
3. Beekman FJ, Kamphuis C, Frey EC. Scatter compensation methods in 3D iterative reconstruction: a simulation study. Phys Med Biol 1997;42:1619–32.
4. Meikle SR, Hutton BF, Bailey DL. A transmission-dependent method for scatter correction in SPECT. J Nucl Med 1994; 35:360–7.
5. Iida H, Narita Y, Kado H, Kashikura A, Sugawara S, Shoji Y, et al. Effects of scatter and attenuation correction on quantitative assessment of regional cerebral blood flow with SPECT. J Nucl Med 1998;39:181–9.
6. Kim KM, Varrone A, Watabe H, Shidahara M, Fujita M, Innis RB, et al. Contribution of scatter and attenuation compensation to SPECT images of nonuniformly distributed brain activities. J Nucl Med 2003;44:512–9.
7. Hutton BF, Osiecki A, Meikle SR. Transmission-based scatter correction of 180° myocardial single-photon emission tomographic studies. Eur J Nucl Med 1996;23:1300–8.
8. Hutton BF, Baccarne V. Efficient scatter modelling for incorporation in maximum likelihood reconstruction. Eur J Nucl Med 1998;25:1658–65.
9. Bowsher JE, Floyd CE. Treatment of Compton scattering in maximum-likelihood expectation maximization reconstructions of SPECT images. J Nucl Med 1991;32:1285–91.
10. Hudson HM, Larkin RS. Accelerated image reconstruction using ordered subsets of projection data. IEEE Trans Med Imaging 1994;13:601–9.
11. Zeng GL, Gullberg GT. Frequency domain implementation of the three-dimensional geometric point response correction in SPECT imaging. IEEE Trans Nucl Sci 1992;39:1444–53.
12. Zeng GL, Gullberg GT, Bai C, Christian PE, Trisjono F, Di Bella EVR, et al. Iterative reconstruction of fluorine-18 SPECT using geometric point response correction. J Nucl Med 1998; 39:124–30.
13. Kadrmas DJ, Frey EC, Karimi SS, Tsui BMW. Fast implementations of reconstruction-based scatter compensation in fully 3D SPECT image reconstruction. Phys Med Biol 1998;43: 857–73.
14. Ljungberg M, Strand SE. A Monte Carlo program for the simulation of scintillation camera characteristics. Comput Methods Programs Biomed 1989;29:257–72.
15. Zubal IG, Harrell CR, Smith EO, Rattner Z, Gindi G, Hoffer PB. Computerized three-dimensional segmented human anatomy. Med Phys 1994;21:299–302.

16. Kim KM, Watabe H, Shidahara M, Ishida Y, Iida H. SPECT collimator dependency of scatter and validation of transmission-dependent scatter compensation methodologies. IEEE Trans Nucl Sci 2001;48:689–96.
17. Di Bella EVR, Barclay AB, Eisner RL, Schafer RW. A comparison of rotation-based methods for iterative reconstruction algorithms. IEEE Trans Nucl Sci 1996;43:3370–6.
18. Beekman FJ, de Jong HW, van Geloven S. Efficient fully 3-D iterative SPECT reconstruction with Monte Carlo-based scatter compensation. IEEE Trans Med Imaging 2002;21: 867–77.
19. Frey EC, Ju ZW, Tsui BMW. A fast projector-backprojector pair modeling the asymmetric, spatially varying scatter response function for scatter compensation in SPECT imaging. IEEE Trans Nucl Sci 1993;40:1192–7.

IOP PUBLISHING PHYSICS IN MEDICINE AND BIOLOGY

Phys. Med. Biol. 53 (2008) N277–N285 doi:10.1088/0031-9155/53/14/N02

NOTE

Acceleration of Monte Carlo-based scatter compensation for cardiac SPECT

A Sohlberg[1,2], H Watabe[1] and H Iida[1]

[1] National Cardiovascular Center Research Institute, 5-7-1 Fujishiro-dai, Suita City, 565-8565 Osaka, Japan
[2] HERMES Medical Solutions, Skeppsbron 44, 111 30 Stockholm, Sweden

E-mail: antti.sohlberg@hermesmedical.com

Received 12 December 2007, in final form 20 May 2008
Published 23 June 2008
Online at stacks.iop.org/PMB/53/N277

Abstract

Single proton emission computed tomography (SPECT) images are degraded by photon scatter making scatter compensation essential for accurate reconstruction. Reconstruction-based scatter compensation with Monte Carlo (MC) modelling of scatter shows promise for accurate scatter correction, but it is normally hampered by long computation times. The aim of this work was to accelerate the MC-based scatter compensation using coarse grid and intermittent scatter modelling. The acceleration methods were compared to un-accelerated implementation using MC-simulated projection data of the mathematical cardiac torso (MCAT) phantom modelling ^{99m}Tc uptake and clinical myocardial perfusion studies. The results showed that when combined the acceleration methods reduced the reconstruction time for 10 ordered subset expectation maximization (OS-EM) iterations from 56 to 11 min without a significant reduction in image quality indicating that the coarse grid and intermittent scatter modelling are suitable for MC-based scatter compensation in cardiac SPECT.

1. Introduction

The quality of single proton emission computed tomography (SPECT) is degraded by attenuation, collimator blurring and scatter. Whereas attenuation and collimator blurring can nowadays be corrected in clinically acceptable times, accurate and efficient scatter correction has been proven to be a more difficult problem. This is mainly due to the fact that the shape of the scatter point-spread function depends on the location inside the object and can be very difficult to parametrize.

One very promising recently presented scatter compensation method is the Monte Carlo (MC)-based scatter correction by Beekman *et al* (2002). In this method, a MC simulator is used as a forward-projector for scatter in the ordered subset expectation maximization

0031-9155/08/140277+09$30.00

(OS-EM) algorithm (Hudson and Larkin 1994). MC-based scatter modelling is expected to be especially advantageous in areas where the attenuating media is highly non-uniform such as the thorax, because it can faithfully produce the complex shape of the scatter response function. The MC-based scatter compensation has been shown to outperform the common triple-energy window scatter compensation method in terms of contrast and myocardial lesion detectability (Xiao *et al* 2006). Unfortunately, despite the considerable advances made in MC-based scatter compensation its widespread utilization in clinical practice can still be limited by long computation times.

Kadrmas *et al* (1998) have presented two simple and effective acceleration methods for reconstruction-based scatter compensation. The first of these approaches is the coarse grid scatter modelling method, which calculates the scatter contribution using sparser grid than is used in the actual reconstruction. The second approach is the intermittent scatter modelling method, where scatter is modelled only during the first couple of OS-EM iterations and then held as a constant additive factor for the later iterations. Both of these approaches are based on the assumption that the scatter response contains mainly low-frequency components and can thus be modelled with a relatively large voxel size and not during the last OS-EM iterations. Kadrmas *et al* presented their acceleration methods for the effective scatter source estimation method (Frey and Tsui 1996) and showed that the performance of the accelerated scatter compensation was very similar to the performance of the standard (un-accelerated) scatter correction.

The goal of this work was to implement the coarse grid and intermittent scatter modelling methods for MC-based scatter compensation and to evaluate their performance in case of ^{99m}Tc cardiac SPECT.

2. Materials and methods

2.1. Implementation of the MC simulator

MC simulations are based on sampling radioactive decays within a source volume and following their interactions inside the attenuating media. Our MC simulator uses four different maps in the simulations: emission map for setting photons to be tracked, density map for sampling interactions and primary and scatter maps for storing photon weights. The history of each photon (primary or scatter) in our simple MC simulator is tracked shortly as follows:

(1) If the simulated photon is a primary the primary map is updated. Otherwise direction cosines are sampled and random walk is started for the scatter photon.

(2) Photon interaction points are calculated using the delta scattering algorithm (Woodcock *et al* 1965), which does not require ray tracing through the attenuating media. The basic principle of delta scattering is that the path-length P between two 'fictious' interaction points is sampled as $P = -\ln(R)/\mu_{max}$, where R is a uniform random number and μ_{max} is the largest attenuation coefficient in the attenuating media (Ljungberg *et al* 2005). At the end of the sampled path a possible interaction is sampled according to established methods or tracking is continued by sampling a new distance P according to the above-mentioned equation.

(3) At each real interaction point photon weight is multiplied by the probability that no photoelectric effect occurred and a copy of the original photon is forced to Compton scatter towards the detector and scatter map is updated according to the convolution-based forced detection approach (de Jong *et al* 2001).

(4) If predetermined number of scattering events has not been reached, the history of the original photon is continued by Compton scatter. New direction cosines are sampled from the Klein–Nishina function and tracking is continued from (2).

After all the photons have been simulated the primary and scatter maps are multiplied by probability that photon emitted from a certain voxel reaches the detector without interaction. Then these maps are convolved with depth-dependent detector response function, which is assumed to be Gaussian. The blurred primary and scatter maps are finally forward-projected to primary and scatter projections.

2.2. *Implementation of the reconstruction algorithm with MC-based scatter compensation*

The developed MC simulator was included into an OS-EM reconstruction algorithm as forward-projector for the scattered counts as originally proposed by Beekman *et al* (2002). The OS-EM is given by

$$f_j^{\text{new}} = \frac{f_j^{\text{old}}}{\sum_{i \in S_n} a_{ij}} \sum_{i \in S_n} a_{ij} \frac{p_i}{\sum_k a_{ik} f_k^{\text{old}} + s_i}, \tag{1}$$

where f is the reconstructed image, p is the measured projections, j (or k) is the reconstruction voxel index, i is the projection pixel index, a_{ij} is the probability that emission from voxel j is detected in pixel i, s is the MC-based scatter projections and S_n is the nth subset. The image update in OS-EM consists of sequential forward- and back-projection operations. The estimated projections are obtained by forward-projecting the current image estimate $\left(\sum_k a_{ik} f_k^{\text{old}}\right)$, and correction terms that are used to update the old image are formed by back-projecting the ratio of the measured and estimated + scatter projections $\left(\sum_{i \in S_n} a_{ij} \frac{p_i}{\sum_k a_{ik} f_k^{\text{old}} + s_i}\right)$.

In this work the forward- and back-projectors were implemented as rotation based (Di Bella *et al* 1996). The back-projector included attenuation and detector response compensation and the forward-projector attenuation, detector response and MC-based scatter compensation. Attenuation correction factors for each voxel were calculated simply by summing the rotated attenuation map along columns. Detector response, on the other hand, was modelled by convolving each plane of the reconstruction matrix parallel to the projection plane with collimator response kernel, which was assumed to be Gaussian. The scatter projection for each projection angle was obtained by MC-based forward-projection of the current image estimate.

2.3. *Acceleration of MC-based scatter compensation*

The coarse grid scatter modelling method was implemented by simply down-sampling the current image estimate (and the attenuation map) into a sparser matrix before the MC-based forward-projection and linearly interpolating the scatter projections back to the original size after forward-projection was finished. In the intermittent acceleration approach the MC-based scatter modelling is performed only in the few early OS-EM iterations and after that the scatter projections are kept fixed for remaining iterations.

2.4. *Performance tests*

Performance tests were performed using a female version of the mathematical cardiac torso (MCAT) phantom (Tsui *et al* 1994), and the camera parameters are shown in table 1. The MCAT phantom modelled normal human tissue densities in the thorax region and the source distribution presented the ^{99m}Tc uptake with the following relative activities per

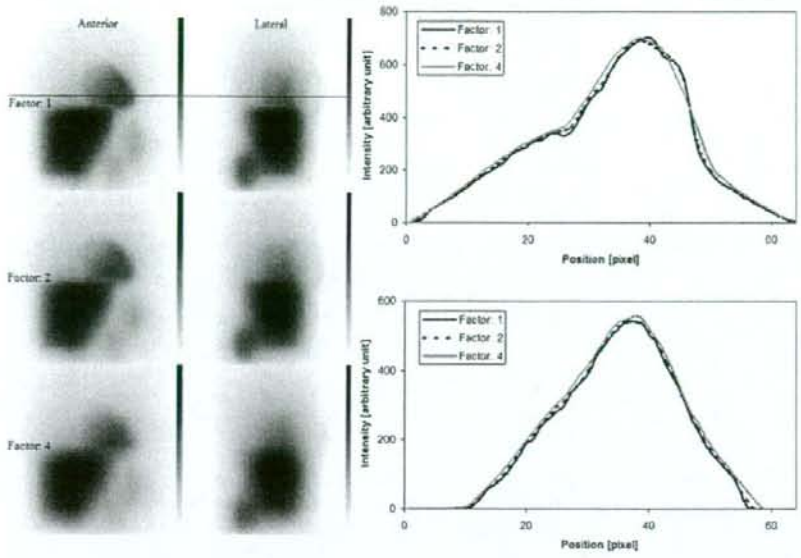

Figure 1. Comparison of scatter projections and profiles obtained with different down-sampling factors (factor: 1 is scatter projection without down-sampling). Upper profile is obtained from the anterior projection and lower from the lateral projection. Locations of the profiles are shown as horizontal lines.

Table 1. Camera parameters for Monte Carlo simulations.

Low-energy high-resolution collimator (4.0 cm hole length, 0.178 cm hole diameter)
0.4 cm intrinsic detector resolution
9.0% energy resolution
15.0% energy window centred on 140 keV
23.0 cm radius of rotation

voxel: myocardium 100, liver 50, kidney 100, spleen 80, lung 5 and rest of the body 2.5. Two lesions (anterior and inferior) with the relative uptake of 2.5 were included in the left myocardium.

The effects of different down-sampling factors in the coarse grid scatter modelling scheme were studied by performing MC simulations using the MCAT phantom. The pixel size was set to 0.625 cm (64 × 64 projection and 64 × 64 × 64 image matrix size). Down-sampling factors of 2 (64 × 64 × 64 image matrix down-sampled to 32 × 32 × 32 matrix) and 4 (64 × 64 × 64 image matrix down-sampled to 16 × 16 × 16 matrix size) were investigated. Figure 1 presents anterior and lateral scatter projection images of the MCAT phantom. According to this figure factor 4 produces slightly distorted scatter projections, and thus the down-sampling factor was set to 2 for all the reconstructions accelerated with the coarse grid scatter modelling.

The effect of the number of scatter update iterations was studied by using MCAT projection data simulated using the SIMIND MC simulator (Ljungberg and Strand 1989). The camera parameters for this simulation are again shown in table 1. The number of simulated noise-free

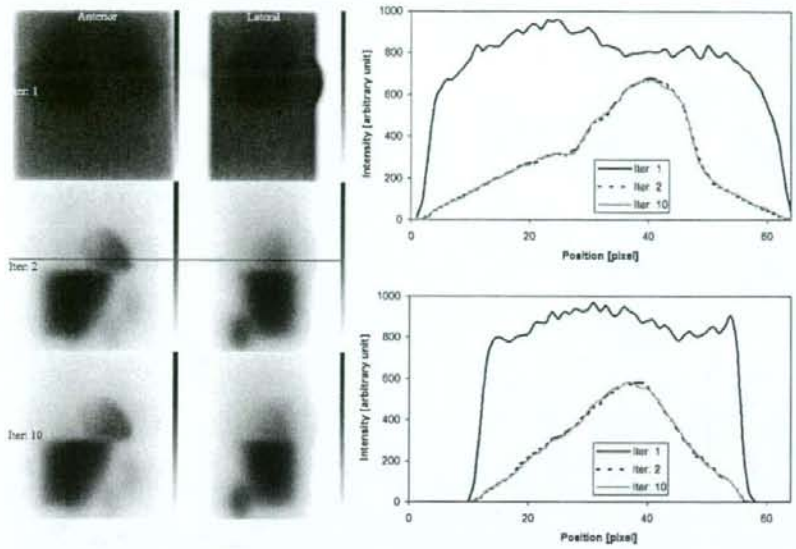

Figure 2. Comparison of different number of scatter update iterations. Upper profile is obtained from the anterior projection and lower from the lateral projection. Locations of the profiles are shown as horizontal lines.

projections was 64 on a 360° orbit and pixel size was 0.3125 cm (128 × 128 projection and 128 × 128 × 128 image matrix size). The projections were collapsed to a 64 × 64 matrix size before the reconstruction. Reconstruction using the noise-free projection data was performed with 16 subsets and 1–10 iterations, and the MC forward-projected scatter projections were saved after every iteration. Figure 2 presents scatter projection images and profiles for different iteration numbers, and these images show that the scatter projections do not change markedly after two iterations. Therefore, in the following performance tests only two scatter iterations were used when intermittent scatter modelling was applied.

The acceleration methods were tested using the same MCAT projection data that were used to find the scatter iterations stopping point. Poisson noise was added to the noise-free projections by setting number of total counts to 5 million. The projections were reconstructed without scatter compensation, with the MC-based scatter compensation but without acceleration, with coarse grid scatter modelling (down-sampling factor of 2), with intermittent scatter modelling (scatter updated during the first two iterations) and with both accelerations applied at the same time. Number of MC simulated photons per projection angle was set to 1.0 million and 16 subsets with 10 iterations were used. After reconstruction images were filtered with a 3D Butterworth filter (order: 5, cutoff: 1.0 cm^{-1}), transverse slices were zoomed and reoriented into short-axis slices. Regions of interest (ROI) were drawn on the normal myocardium, ventricle and on the anterior/inferior defect areas. Normal myocardium to ventricle and normal myocardium to lesion contrasts were calculated.

In addition to Monte Carlo simulations the acceleration methods were also tested using a clinical ^{99m}Tc myocardial stress/rest perfusion study acquired with the Siemens Symbia SPECT/CT scanner. Low-energy high-resolution parallel hole collimators were used, and

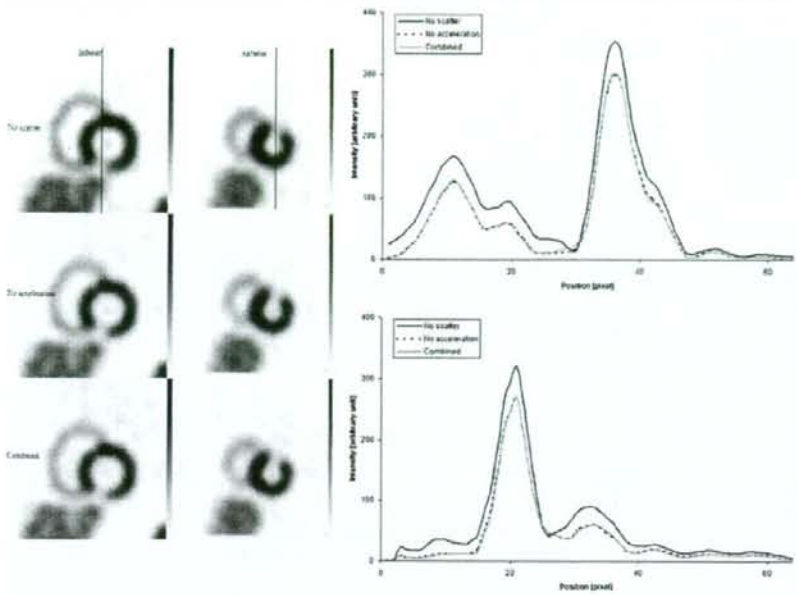

Figure 3. Short-axis slices and profiles through the heart of the MCAT phantom for reconstruction without scatter compensation (no scatter) and with MC-based scatter compensation without acceleration (no acceleration) and with coarse grid + intermittent scatter modelling (combined). Results for other acceleration methods are not shown, because they overlap the coarse grid + intermittent scatter compensation profiles. Upper profile is obtained from the image with inferior lesion and lower with anterior lesion. Locations of the profiles are shown as vertical lines.

Table 2. Lesion-to-normal myocardium and ventricle-to-normal myocardium contrasts for different MC-based scatter compensation acceleration schemes.

Scatter compensation method	Acceleration method	Contrast		
		Anterior	Inferior	Ventricle
No compensation		0.57	0.51	0.80
MC-based	No acceleration	0.64	0.58	0.91
	Coarse grid	0.65	0.59	0.93
	Intermittent	0.62	0.60	0.93
	Coarse grid+intermittent	0.64	0.59	0.93

60 projection angles over a 180° arc were acquired using a symmetric 15% energy window centred at 140 keV.

3. Results

Figure 3 shows short-axis slices and profiles through the left ventricle of the MCAT phantom for reconstruction without scatter compensation and with the MC-based scatter compensation without acceleration and with coarse grid + intermittent scatter modelling. Profiles for the

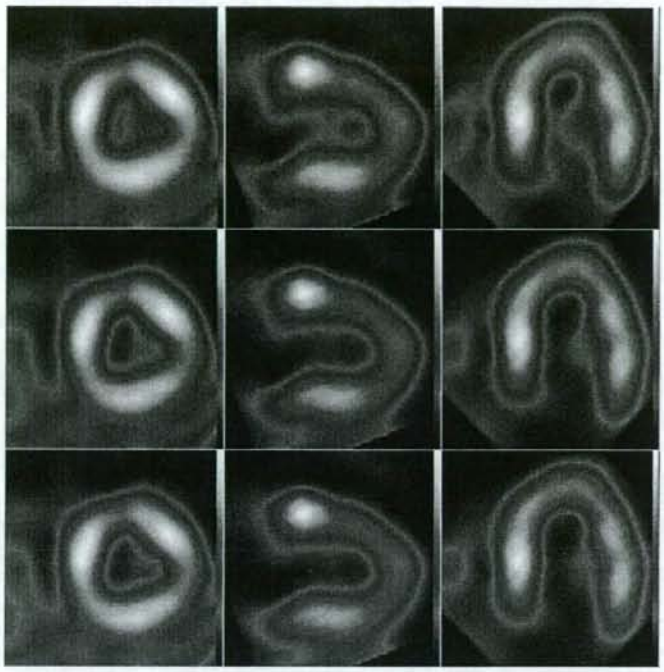

Figure 4. Example short-axis (first column), vertical long-axis (second column) and horizontal long-axis (third column) slices from a clinical rest myocardial perfusion study for reconstruction without scatter compensation (first row), with MC-based scatter compensation without acceleration (second row) and with coarse grid +intermittent scatter modelling (third row).

un-accelerated and accelerated scatter compensation practically overlap indicating similar performance. This same conclusion can also be drawn from table 2, which presents the lesion and ventricle contrasts. All the scatter compensation methods offer very similar contrast values and clearly improve contrast when compared to reconstruction without scatter compensation.

Figure 4 presents results for the resting clinical study (for the stress study the findings in image quality were identical to the resting study). It can be seen that the images reconstructed with and without MC-based scatter compensation acceleration are nearly identical. Table 3 presents the approximate reconstruction times for different scatter compensation methods.

4. Discussion

The aim of this study was to accelerate the MC-based scatter compensation using the coarse grid and intermittent scatter modelling methods. Both of these acceleration methods proved to provide clear improvement in execution times without any marked degradation in image quality when compared to un-accelerated version of MC-based scatter-compensation (tables 2 and 3, figures 3 and 4). The greatest improvement in terms of speed was obtained by combining the two acceleration methods.

Table 3. Approximate reconstruction times (10 iterations, 16 subsets and 1 million photons per projection) for different MC-based scatter compensation acceleration schemes. Reconstructions were performed using 2.33 GHz Pentium processor with 8 GB RAM.

Scatter compensation method	Acceleration method	Time (min)
No compensation		0.8
MC-based	No acceleration	55.6
	Coarse grid	53.4
	Intermittent	11.6
	Coarse grid + intermittent	11.2

The comparison studies for the scatter compensation methods were performed with $64 \times 64 \times 64$ matrix sizes and coarse-grid down-sampling factor of 2 was used, because larger down-sampling factors could not fully preserve the details of the scatter projections (figure 1). With larger matrix sizes than $64 \times 64 \times 64$ larger down-sampling factors could probably be used for higher acceleration. This was not studied in this work, because in the case of cardiac SPECT $64 \times 64 \times 64$ matrix size is usually considered the standard.

The acceleration achieved with the coarse grid scatter modelling depends also on the implementation of the MC simulator that is used in the forward-projection. As mentioned, our MC simulator is based on the delta scattering technique (Woodcock *et al* 1965), which allows calculation of the photon interaction points without time-consuming ray tracing. Therefore, the coarse-grid scatter modelling provided acceleration mainly because the collimator response and attenuation modelling were performed with the sparser matrix. In the case of 1 million simulated photons per projection the time needed to model the collimator response and attenuation is, however, only a small fraction of the time that is spent in sampling the various probability distributions in the MC calculations. Thus the speed-up provided by the coarse-grid scatter modelling is quite small, but can be much greater if a smaller number of simulated photons are used. In addition, if a ray-tracing-based MC algorithm is used instead of delta scattering, coarse-grid scatter modelling will probably increase the speed much more, because the efficiency of ray tracing depends heavily on the matrix size.

In this study the scatter projections were not noticed to change markedly after two iterations, and thus in the intermittent scatter modelling scheme scatter projections were updated only during the first two OS-EM iterations. The number of scatter iterations needed may, however, depend on the imaging situation as mentioned by Kadrmas *et al* (1998) and should therefore be checked before using intermittent scatter modelling as an acceleration method.

One important thing that was not considered in detail in this work is the number of simulated photons per projection. We chose the 1 million photons per projection according to our preliminary studies, where we compared the quality of images reconstructed using different number of simulated photons and noticed that using over 1 million photons per projection does not lead to a significant increase in image quality. The performance of MC-based scatter compensation is, however, quite complicated because it is not only influenced by the number of simulated photons but also by the interplay of noise in attenuation map/projection data and the number of simulated photons. Therefore, a detailed study of noise effects, e.g. similar to the one presented by de Wit *et al* (2005), is probably needed in the future. If different number of photons per projection are to be used the speed-up factors might not be the same as in table 2.

Faster reconstruction times with MC-based scatter compensation than those shown in table 3 have been presented in the literature (e.g. de Wit *et al* (2005) and Xiao *et al* (2006)). This

speed difference is probably mainly related to algorithm implementation. Our reconstruction algorithm is not yet fully optimized, and we believe that we can greatly reduce the execution time of our reconstruction. In addition to direct code optimization, we are also planning to parallelize our code for multi-core processors. The acceleration methods presented in this work should be very suitable for different parallelization schemes, because they do not affect the general structure of the OS-EM reconstruction algorithm.

5. Conclusions

We conclude that both the coarse grid and the intermittent scatter modelling methods are suitable for accelerating MC-based scatter compensation, and with these methods MC-based scatter compensation is a promising alternative for clinical cardiac SPECT.

Acknowledgment

This work was supported by grants from the Japan Society for the Promotion of Science.

References

Beekman F J, de Jong H W A M and van Geloven S 2002 Efficient fully 3-D iterative SPECT reconstruction with Monte Carlo-based scatter compensation *IEEE Trans. Med. Imaging* **21** 867–77

de Jong H W A M, Slijpen E T P and Beekman F J 2001 Acceleration of Monte Carlo SPECT simulation using convolution-based forced detection *IEEE Trans. Nucl. Sci.* **48** 58–64

de Wit T C, Xiao J and Beekman F J 2005 Monte Carlo-based statistical SPECT reconstruction: influence of number of photon tracks *IEEE Trans. Nucl. Sci.* **52** 1365–9

Di Bella E V R, Barclay A B, Eisner R L and Schafer R W 1996 A comparison of rotation-based methods for iterative reconstruction algorithms *IEEE Trans. Nucl. Sci.* **43** 3370–6

Frey E C and Tsui B M W 1996 A new method for modelling the spatially-variant, object dependent scatter response function in SPECT *IEEE Nuclear Science Symp.and Medical Imaging Conf. Record* pp 1082–6

Hudson H M and Larkin R S 1994 Accelerated image reconstruction using ordered subsets of projection data *IEEE Trans. Med. Imaging* **13** 601–9

Kadrmas D J, Frey E C, Karimi S S and Tsui B M W 1998 Fast implementations of reconstruction-based scatter compensation in fully 3D SPECT image reconstruction *Phys. Med. Biol.* **43** 857–73

Ljungberg M, Larsson A and Johansson L 2005 A New collimator simulation in SIMIND based on the Delta-Scattering technique *IEEE Trans. Nucl. Sci.* **52** 1370–5

Ljungberg M and Strand S-E 1989 A Monte Carlo program for the simulation of scintillation camera characteristics *Comput. Methods Programs Biomed.* **29** 257–72

Tsui B M W, Zhao X D, Gregoriou G K, Lalush D S, Frey E C, Johnston R E and McCartney W H 1994 Quantitative cardiac SPECT reconstruction with reduced image degradation due to patient anatomy *IEEE Trans. Nucl. Sci.* **41** 2838–44

Woodcock E, Murphy T, Hemmings P and Longworth S 1965 Techniques used in the GEM code for Monte Carlo neutronics calculations in reactors and other systems with complex geometry *Proc. Conf. for Applications of Computing Methods to Reactor Problems* p 557

Xiao J, de Wit T C, Staelens S G and Beekman F J 2006 Evaluation of 3D Monte Carlo-based scatter correction for ^{99m}Tc cardiac perfusion SPECT *J. Nucl. Med.* **47** 1662–9

Use of a Clinical MRI Scanner for Pre-clinical Research on Rats

Akihide YAMAMOTO [1,2], Hiroshi SATO[3], Jun-ichiro ENMI[1],Kenji ISHIDA[1], Takayuki OSE[1], Atsuomi KIMURA[2], Hideaki FUJIWARA[2], Hiroshi WATABE[1,2], Takuya HAYASHI[1,2], Hidehiro IIDA[1,2] *

1. Department of Investigative Radiology, Advanced Medical-Engineering Center, National Cardiovascular Center-Research Institute, 5-7-1, Fujishiro-dai, Suita, Osaka, 565-8565, Japan.
2. Department of Medical Physics and Engineering, Division of Health Sciences, Graduate School of Medicine, Osaka University, 1-7, Yamada-oka, Suita, Osaka, 565-0871, Japan.
3. Laboratory for Diagnostic Solution, Advanced Medical-Engineering Center, National Cardiovascular Center-Research Institute, 5-7-1, Fujishiro-dai, Suita, Osaka, 565-8565, Japan.

*Corresponding author: Hidehiro Iida, D.Sc., Ph.D.
Department of Investigative Radiology, Advanced Medical-Engineering Center,
National Cardiovascular Center-Research Institute
*5-7-1, Fujishiro-dai, Suita, Osaka, 565-8565, Japan
Phone: +81-6-6833-5012 ex 2559, Fax: +81-6-6835-5429, iida@ri.ncvc.go.jp

RUNNING HEAD: Use of a 3-Tesla MRI Scanner for rat brain imaging

Key Words:
Quantitative mapping; human whole-body 3-Tesla MRI scanner; single dose of Gd-DTPA; dynamic susceptibility contrast (DSC); pre-clinical research; rat brain

Abstract (150words)

This study focused on evaluating the feasibility of rat brain imaging by use of a human whole-body 3-Tesla magnetic-resonance-imaging (MRI) scanner with developed transmit-and-receive radiofrequency coils.

The T_1-, T_2- weighted images obtained showed reasonable contrast. Acquired contrast-free time-of-flight magnetic-resonance-angiography images clearly showed the cortical middle-cerebral-artery (MCA) branches, and inter-hemispheric differences could be observed.

Dynamic-susceptibility-contrast MRI at a 1.17 mm^3 voxel resolution, performed three times following administration of gadolinium-diethylenetriamine pentaacetic acid (Gd-DTPA, 0.1 mmol/kg), demonstrated that the arterial input function (AIF) can be obtained from the MCA region, yielding cerebral blood flow (CBF), cerebral blood volume, and mean transit time (MTT) maps. The parietal-cortex (Pt)-to-hypothalamus (HT) CBF ratio was 45.11 ± 2.85 %, and the MTT was 1.29 ± 0.40 sec in the Pt and 2.32 ± 0.17 sec in the HT region. A single dose of Gd-DTPA enabled assessment of AIF within the MCA territory and of quantitative CBF in rats.

Introduction

Magnetic-resonance-imaging (MRI) has been widely used in pre-clinical research on experimental small animals. Studies have typically been aimed at understanding the pathophysiologic status and for evaluating the efficacy/side effects of newly developed treatments, such as pharmaceutical and regenerative medicine. Recently, a different idea has surfaced: the use of a human whole-body MRI scanner for small-animal imaging [1]. Although small-animal dedicated scanners are superior to clinical scanners in terms of providing a better signal-to-noise ratio, the available pulse sequences are different from those on clinical scanners, and the magnetic field strength is often much higher. Small-animal imaging with clinical scanners is important for directly addressing clinical questions and/or identifying the source of signal changes, including various disease conditions in a clinical setting.

Smith et al. [2] demonstrated that anatomic brain T_1- weighted (T_1W) images and T_2-weighted (T_2W) images can be obtained for healthy rats by use of a 1-Tesla clinical MRI scanner with a specially designed radiofrequency (RF) coil, given a reasonable spatial resolution ($0.1953 \times 0.1953 \times 2.5$ mm, 24 min of T_1W and 48 min of T_2W). The image contrast was sufficiently high for distinguishing the cortical gray matter from the white matter (corpus callosum (CC)), as well as the lateral ventricle (LV) and interpeduncular cistern (IPC) from the thalamus (Thal). Guzman et al. [3] employed a clinical 1.5-Tesla MRI scanner with a commercially available RF coil and demonstrated that both T_1W and T_2W images can be obtained with good contrast, a

reasonable spatial resolution of 0.3125 × 0.3125 × 1.5 mm, and an acquisition time of 19 min 51 sec, as well as 0.35156 × 0.375 × 1.5 mm at 8 min 34 sec, corresponding to T_1W and T_2W images, respectively. Other investigators [4] applied a clinical 1.5-Tesla MRI scanner with a 3-inch-diameter circular receive-only surface coil to assess anatomic images. Their images can be of use in the evaluation of the pathophysiologic status of stroke [4] and cancer [5, 6], as well as the effects of neural excitotoxicity [3]. There were also several studies with a clinical 3-Tesla MRI scanner fitted with commercial and/or hand-made RF coils for investigating the pathophysiology of stroke [7, 8] and brain tumors in rats [6, 9, 10]. Generally speaking, anatomic images with better contrast can be obtained in a stronger magnetic field, although there are additional factors which may influence the signal-to-noise ratio (SNR) or spatial resolution of anatomic images. Contrast-free time-of-flight magnetic-resonance angiography (TOF-MRA) can also be obtained on rats with a reasonable spatial resolution by use of a clinical 3-Tesla MRI scanner with a single-turn solenoid coil [11].

Dynamic-susceptibility-contrast MRI (DSC-MRI) [12] has been widely used in clinical diagnosis, particularly in patients with stroke [13-19] and tumors [20]. The application of clinical MRI scanners has been extended to DSC-MRI studies of small-animals with stroke [21, 22] and tumors [23] by use of a 1.5-Tesla MRI scanner. Up to now, small-animal studies have been performed on 1.5-Tesla MRI scanners only, and 3-Tesla scanners have not yet been employed. This is largely attributed to

the fact that the susceptibility-induced inhomogeneous magnetic field may cause more serious distortion of the images at a higher static magnetic field. In DSC-MRI studies, the echo planar imaging (EPI) technique is mainly used because fast acquisition is required for accurate tracking of the bolus passage of MR contrast agents. The EPI technique, however, is very sensitive to magnetic field inhomogeneity, and thus the EPI images of small-animal brains may be severely distorted. The gradient slew rate (SR) is not high enough to support sufficiently short echo spacing period, when clinical scanners are used for high-spatial resolution imaging of small objects. Moreover, injected materials may cause further distortion [24]. Currently, it is unknown how severely dynamic EPI images of small-animal brains will become distorted on a 3-Tesla clinical scanner. The arterial input function (AIF) is also questionable. To the best of our knowledge, no DSC-MRI studies of small-animal brains on 3-Tesla clinical scanners have been reported.

This study was aimed at evaluating the feasibility of a human whole-body 3-Tesla MRI system developed for small animals, particularly for DSC-MRI with a single dose of gadolinium-diethylenetriamine pentaacetic acid (Gd-DTPA). The quality of various images, including the anatomic T_1W images, T_2W images, TOF-MRA images, and DSC images, was tested, and the availability of the AIF obtained from the rat brain was evaluated.

Materials and Methods

Subjects

The subjects were three healthy adult rats supplied by Japan SLC, Inc. (Shizuoka, Japan). All three rats were males, and they ranged in age from 20 to 24 weeks. Their weight range was between 400 to 600 grams. Anesthesia was administered with an intramuscular injection of ketamine (33 mg/kg; Daiichi-Sankyo Co., Ltd., Tokyo, Japan) and xylazine (6.6 mg/kg; Bayer Yakuhin, Ltd., Osaka, Japan). The first rat (Sprague-Dawley, SD) was used for T_1-W and T_2W imaging of the whole brain. The second rat, also a SD, was used for contrast-free TOF-MRA imaging. The third was a Wistar rat, which was used for a Gd-DTPA (0.1 mmol/kg; Bayer Yakuhin, Ltd., Osaka, Japan)-enhanced DSC-MRI sequence. Experiments were carried out according to the protocol approved by the Local Committee for Laboratory Animal Welfare, National Cardiovascular Center, Osaka, Japan.

MRI acquisition

A human whole-body 3-Tesla MRI scanner (Signa, GE Healthcare, Milwaukee, WI, USA) equipped with a 55-cm bore was employed in this study. The gradient coil system was capable of providing the maximum amplitude of the gradient at 40 mT/m, and at an SR of 150 T/m/s. All sequence programs employed in this study were designed for clinical studies.

Two solenoid coils designed for rats were specially developed to cover the whole brain, which are capable of both transmitting and receiving RF pulses. The three-turn solenoid coil, which had a diameter of 42 mm and a length along a cylindrical axis of 18 mm, was attached to an apparatus made of acrylic mold as